Logarithmic total variation regularization via preconditioned conjugate gradient method for sparse reconstruction of bioluminescence tomography

Gege Zhang [a,b], Jun Zhang [a,b], Yi Chen [a,b], Mengfei Du [a,b], Kang Li [a,b], Linzhi Su [a,b], Huangjian Yi [a], Fengjun Zhao [a], Xin Cao [a,b,*]

[a] School of Information Science and Technology, Northwest University, Xi'an, Shaanxi 710127, China
[b] National and Local Joint Engineering Research Center for Cultural Heritage Digitization, Xi'an, Shaanxi 710127, China

ARTICLE INFO

ABSTRACT

Background and objective: Bioluminescence Tomography (BLT) is a powerful optical molecular imaging technique that enables the noninvasive investigation of dynamic biological phenomena. It aims to reconstruct the three-dimensional spatial distribution of bioluminescent sources from optical measurements collected on the surface of the imaged object. However, BLT reconstruction is a challenging ill-posed problem due to the scattering effect of light and the limitations in detecting surface photons, which makes it difficult for existing methods to achieve satisfactory reconstruction results. In this study, we propose a novel method for sparse reconstruction of BLT based on a preconditioned conjugate gradient with logarithmic total variation regularization (PCG-logTV).
Method: This PCG-logTV method incorporates the sparsity of overlapping groups and enhances the sparse structure of these groups using logarithmic functions, which can preserve edge features and achieve more stable reconstruction results in BLT. To accelerate the convergence of the algorithm solution, we use the preconditioned conjugate gradient iteration method on the objective function and obtain the reconstruction results. We demonstrate the performance of our proposed method through numerical simulations and *in vivo* experiment.
Results and conclusions: The results show that the PCG-logTV method obtains the most accurate reconstruction results, and the minimum position error (LE) is 0.254mm, which is 26%, 31% and 34% of the FISTA (0.961), IVTCG (0.81) and L_1-TV (0.739) methods, and the root mean square error (RMSE) and relative intensity error (RIE) are the smallest, indicating that it is closest to the real light source. In addition, compared with the other three methods, the PCG-logTV method also has the highest DICE similarity coefficient, which is 0.928, which means that this method can effectively reconstruct the three-dimensional spatial distribution of bioluminescent light sources, has higher resolution and robustness, and is beneficial to the preclinical and clinical studies of BLT.

1. Introduction

Bioluminescence imaging (BLI) is a rapidly developing optical molecular imaging technique that utilizes intrinsic optical signals generated by the organism without the need for external stimulation [1]. BLI can provide two-dimensional planar signals, but it cannot capture essential information such as the three-dimensional position and shape of the light source [2]. To better locate and quantify the three-dimensional distribution of bioluminescent sources *in vivo*, bioluminescence tomography (BLT) has been developed [3]. BLT can reconstruct the distribution of bioluminescent sources from the measured luminous flux on the surface based on the photon propagation model and visualize the structure and lesions of animals [4,5]. To date, BLT has demonstrated a

range of practical applications, including monitoring physiological processes at molecular and cellular levels [6,7]. Compared to other molecular imaging modalities, BLT has the benefits of low cost, non-invasiveness, and high sensitivity, making it a powerful tool for tumor monitoring and disease pathogenesis research [8–10].

Light source localization and morphological reconstruction pose significant challenges in practical biological applications of BLT. However, BLT is inherently an ill-posed problem due to the scattering effect of light and the limited detection of surface photons. These factors contribute to the poor accuracy of the reconstruction process [11,12]. Therefore, methods to reduce ill-posedness and improve reconstruction accuracy are essential and still under development. In 2004, Wang et al. theoretically demonstrated that the reconstruction problem generally

does not have a unique solution. They highlighted that introducing sufficient prior information is crucial to obtaining a unique solution for the inverse problem [13]. The optical characteristic parameters of internal biological tissue, anatomical structure information of organisms, and the wide-spectrum characteristics of luminous molecular probes are all important prior information for light source reconstruction [14]. Currently, traditional reconstruction algorithms mainly improve the accuracy of reconstruction by introducing a large amount of prior information, such as multimodal strategies combined with CT or MRI [15, 16], sparsity, multispectral data [17–19], feasible light source regions [20], and more. Among these, light source sparsity is a commonly utilized prior information in reconstruction algorithms. Numerous algorithms based on sparse regularization have been proposed and extensively adopted, including: L_2-norm regularization (Tikhonov) [21], L_1-norm regularization (Lasso) [22,23], and L_p-norm (p $\in$ (0, 1)) regularization (non-convex method) [24]. These methods are typically employed to mitigate the ill-posedness of the problem and obtain approximate pseudo-solutions for inverse problems.

Although these algorithms can improve the positioning accuracy of light sources, they also have some drawbacks. For example, applying L_2-norm regularization can result in a reconstruction that is overly smooth [25], and applying L_1/L_p-norm regularization can yield a reconstruction that is excessively sparse [26], which affects the accuracy of light source shape recovery.

Total variation (TV) regularization is a commonly used penalty function in sparse signal processing. It was initially proposed in [27] and has gained significant popularity due to its remarkable ability to preserve edges. TV is widely used in denoising [28–31], deconvolution [32, 33], reconstruction [34], nonlinear decomposition [35], and compression sensing [36]. In practical applications, tumor boundary information and morphological features play a vital role in achieving satisfactory reconstruction. To ensure the preservation of edge information and discontinuities in BLT reconstruction, TV regularization is commonly employed as the penalty function [37,38]. With TV regularization, the emphasis is not on the magnitude of the penalty solution itself, but rather on the magnitude of its variation. Unlike L_2-norm regularization, TV regularization does not smooth edges and sharp transitions, filtering only components with high oscillation and variation. Therefore, TV regularization is expected to provide better resolution and more stable reconstruction than conventional regularization techniques. However, it also has drawbacks. Smooth regions in the original image are recovered as piecewise smooth regions in TV regularization-based solutions, which can introduce trapezoidal artifacts or artificial contours in the image [39].

In this paper, we propose a preconditioned conjugate gradient with a logarithmic total variation regularization method (PCG-logTV) for sparse BLT reconstruction. Our method utilizes Total Variation (TV) regularization as a smoothing penalty function, enabling the preservation of edge information and discontinuities during BLT reconstruction. Additionally, considering the sparse group characteristics of the light source distribution, we assume that the derivative of the bioluminescent source distribution points exhibits not only sparsity but also a structured sparsity in a simple form [40]. Therefore, the PCG-logTV method incorporates the sparsity of overlapping groups and uses a logarithmic function to enhance group structure sparsity [41]. This function allows for larger variance differences within the group and suppresses small estimation components, effectively reducing the occurrence of trapezoidal artifacts commonly observed in TV regularization-based solutions. The preconditioned conjugate gradient (PCG) iteration method is applied to the formulated objective function [42], resulting in a stable reconstruction result. To verify our method, we perform a series of numerical simulations and *in vivo* experiment and compare with the fast iterative shrinkage thresholding algorithm (FISTA) method based on L_1-norm [43], the incomplete variable truncated conjugate gradient (IVTCG) method based on L_1-norm [44], and the regularized reconstruction based on joint L_1 and TV regularization (L_1-TV) method [45].

The experimental results show that our method has achieved satisfactory results in terms of reconstruction quality and accuracy.

The rest of this paper is organized as follows: In Section 2, we introduce the BLT forward model, BLT inverse problem, and PCG-logTV method. In Section 3, we present the specific experiments and results, including numerical simulations and *in vivo* experiment. In Section 4, we discuss and conclude our work.

2. Methodology

2.1. Photon propagation model of BLT

BLT reconstruction using the numerical model-based method usually solves an approximation of the radiative transfer equation (RTE) model, such as the diffusion equation (DE), to obtain the forward result of BLT. The steady-state DE and Robin boundary condition can be written as follows [46]:

$$\begin{cases} -\nabla[D(x)\nabla\Phi(x)] + \mu_\alpha(x)\Phi(x) = S(x), x \in \Omega \\ \Phi(x) + 2\varepsilon D(x)[v(x)\cdot\nabla\Phi(x)] = 0, x \in \partial\Omega \end{cases} \tag{1}$$

where Ω is the domain of the imaged object; $\partial\Omega$ is the boundary of Ω; $S(x)$ is the power density of the internal bioluminescence source; $\Phi(x)$ represents the photon fluence rate; v denotes the unit outer normal at boundary $\partial\Omega$. $D(x)$ represents the diffusion coefficient that can be calculated by $D(x) = 1/3(\mu_\alpha(x) + \mu_s'(x))$, in which $\mu_\alpha(x)$ is the optical absorption coefficient and $\mu_s'(x)$ is the reduced scattering coefficient.

Since the whole process of BLT is conducted in dark and airtight conditions, no light comes from the outside to the imaging environment, so the Robin boundary condition is used, which is given by [47]:

$$\Phi(x) + 2F_{bm}(x; n, n')D(x)[v(x)\nabla\Phi(x)] = 0, x \in \partial\Omega \tag{2}$$

where F_{bm} is the boundary mismatch factor between the biological tissues and the surrounding medium, n is the refractive indices within $\partial\Omega$, n' is the refractive indices of the surrounding medium.

According to the Robin boundary condition, the theoretical value of light intensity density transmitted from the biological body surface can be deduced as follows:

$$\Gamma(x) = -D(x)[v(x)\nabla\Phi(x)] = \frac{\Phi(x)}{2F_{bm}(x; n, n')}, x \in \partial\Omega \tag{3}$$

By applying the variational principle and finite element method to the above photon transmission model, the following linear relationship between the light intensity density distribution on the surface of the born object and the unknown light source distribution in the body can be derived:

$$\Phi_{meas} = AX \tag{4}$$

where X is a $N \times 1$ fluorescence yield, A is a $M \times N$ system matrix, and the known measurement $M \times 1$ vector Φ_{meas} represents the photon density on the surface.

2.2. BLT reconstruction based on PCG-logTV method

The inverse problem based on Eq. (4) can be converted into an optimization problem using the PCG-logTV method. The cost function we aim to minimize consists of two parts: a data-fitting term and a penalty term, as follows:

$$X^* = \underset{X}{argmin}\left\{\frac{1}{2}AX - \Phi_2^2 + \lambda log\left(\varnothing^{TV}(CX)\right)\right\} \tag{5}$$

where λ is the penalty weighting factor, $C \in R_K \times R_N$, with K being the number of pixels in X and N being the number of neighboring pixel pairs. As a penalty item, log-TV regularizer is used to encourage sparse group

structure, allow more variance differences within the group, and suppress small estimated components, thus reducing the trapezoidal artifacts that often occur in solutions based on TV regularization.

TV regularization defined as follows [48]:

$$TV(X) = \sum_K |x_{a(k)} - x_{b(k)}| \approx \sum_K \sqrt{[CX]_k^2 + \delta_{TV}} \quad (6)$$

where $a(k)$ and $b(k)$ are pixel indices corresponding to the kth neighboring pixel pair in the X, δ_{TV} is tends to round off sharp edges when large. The trapezoidal artifacts often occur in TV regularization-based solutions [29]. In order to obtain higher quality reconstruction results, considering the sparse group characteristic of the light source distribution, it is assumed that the bioluminescent light source distribution point has a derivative, which is not only sparse but also a simple form of structured sparse. In this work, we use the function $\varnothing^{TV}$ defined by:

$$\varnothing^{TV}(CX) = \sum_K \left[\sum_{s=0}^{S-1} |v(k+s)|^2 \right]^{1/2} \quad (7)$$

where S is the size of the overlapping group, the transformation $v_k = Cx_k$ computes nearest-neighbor differences. This function is used to promote group sparsity and preserve edges in 3D images.

It is observed that for non-negative parameters, the square root function and logarithm are strictly concave, so any of its tangents are upper bounds; more formally, for any $a \geq 0$ and $a' > 0$, $z \geq 0$ and $z' > 0$:

$$\sqrt{a} \leq \sqrt{a'} + \frac{a - a'}{2\sqrt{a'}}$$

$$log z \leq log z' + \frac{z - z'}{z'} \quad (8)$$

Applying this inequality to $\varnothing^{TV}(CX)$ and logarithm function, the following equations can be obtained:

$$\varnothing^{TV}(CX) = \frac{1}{2} \sum_K \frac{\sum_{s=0}^{S-1} |v(k+s)|^2}{\varnothing^{TV}(CX^t)} + D_1$$

$$log(\varnothing^{TV}(CX)) = \frac{\varnothing^{TV}(CX)}{\varnothing^{TV}(CX^t)} + D_2 \quad (9)$$

where t is the number of iterations, D_1, D_2 stand for a constant independent of X. For the PCG-logTV method, the final optimization function can be expressed as:

$$X^* = \arg\min_X \left\{ \frac{1}{2} AX - \Phi_2^2 + \frac{\lambda}{2\varnothing^{TV}(CX^t)} \sum_K \frac{\sum_{s=0}^{S-1} |v(k+s)|^2}{\varnothing^{TV}(CX^t)} + D \right\} \quad (10)$$

where D stands for a constant independent of X.

To lower the condition number of the system matrix and speed up the convergence of PCG-logTV, the PCG iteration method is employed to derive a computationally efficient, fast converging, algorithm to minimize the cost function in Eq. (10). This method uses the gradient given by:

$$A^T(AX^{t+1} - \Phi) + \lambda C^T diag\left(\frac{1}{(\varnothing^{TV}(CX^t))^2}\right) CX^{t+1} = 0 \quad (11)$$

the above equation can be viewed as $A^t X = b'$, where A^t and b' can be expressed as:

$$A^t = A^T A + \lambda C^T diag\left(\frac{1}{(\varnothing^{TV}(CX^t))^2}\right) C \quad (12)$$

$$b' = A^T \Phi$$

With the PCG iteration method, the preprocessing factor M needs to

Algorithm 1
PCG-logTV

Input: The system matrix A and the measured luminous flux vector Φ.
Initialization: X^0, $t_{max} = 10$, $err = 1e - 5$, $t = 0$, $\lambda = 0.0005$, overlap group size $S = 3$.
Compute: $b' = A^T \Phi, C, A^t$.
While $AX^{t+1} - \Phi_2 > err$ or $t < t\_max$ do
  Step1: $X^{t+1} = X^t$
  Step2: while X^{t+1} does not satisfy PCG stopping criterion do X^{t+1}: PCG iteration for $A^t X = b'$, initialized at X^{t+1}
  end while.
  Step3: $t = t + 1$
  End while
  Output: $X = X^{t+1}$

be introduced first, with the aim of reducing the condition number of the coefficient matrix to speed up the convergence. As for the determination of pretreatment factor M, the super-relaxation method (SOR) is used here, and the specific methods are as follows:

$$W = \begin{cases} \sqrt{\frac{A_{ij}}{\omega}}, (i = j) \\ 0, \ (i \neq j) \end{cases}$$

$$Z = W^{-1}(W^T W + L) \quad (13)$$

$$M = \frac{1}{(2-\omega)} Z^T Z$$

where L is the strictly upper triangular matrix of A, ω is the over-relaxation factor, and the range of values is $0 < \omega < 2$ [49].

Let the initial value of X be X^0, calculate $r^0 = b' - A^t X^0$, and also can solve $Mh^0 = r^0$. Let $p^0 = h^0$, and the number of iterations for calculating $A^t X = b'$ is $d = 1, 2\ldots$, the iterative steps are as follows:

$$\begin{cases} \alpha^d = \frac{(r^d)^T h^d}{(p^d)^T A p^d} \\ X^{d+1} = X^d + \alpha^d p^d \\ r^{d+1} = r^d - \alpha^d A p^{d+1} \\ Mh^{d+1} = r^{d+1} \\ \beta^d = \frac{(r^{d+1})^T h^{d+1}}{(r^d)^T h^d} \\ p^{d+1} = h^{d+1} + \beta^d p^d \end{cases} \quad (14)$$

where X^d is the solution of the equation obtained at each iteration, r^d is the residual at each iteration, and the rest of the variables are process variables at each iteration. The PCG-logTV method combines PCG and logTV to transform the inverse problem into a solution problem for a linear equation system, and effectively solves the linear equation system using the PCG method, thereby improving the overall solution efficiency. However, the performance of the method is often sensitive to the selection of initial solutions and convergence criteria. Based on prior experience, we set the initial solution as: $x^0 = A\dagger y$, and the convergence criterion is set to: $AX^{t+1} - \Phi_2 \leq err$.

Therefore, the complete procedure of the PCG-logTV method for BLT reconstruction is summarized in Algorithm 1. The reconstruction algorithm was implemented using MATLAB (2016a) on a desktop computer with Intel® Core™ i5-1135G7 CPU (2.42 GHz) and 16.0 GB RAM.

3. Experiments and results

In order to evaluate the performance of the PCG-logTV method proposed in Section 2, a series of numerical simulations and one *in vivo* experiment were carried out, and compared with the FISTA, IVTCG, and L_1-TV methods. This section mainly introduces four quantitative evaluation criteria, as well as the specific simulation experiments and *in vivo*

A   **B**   **C**
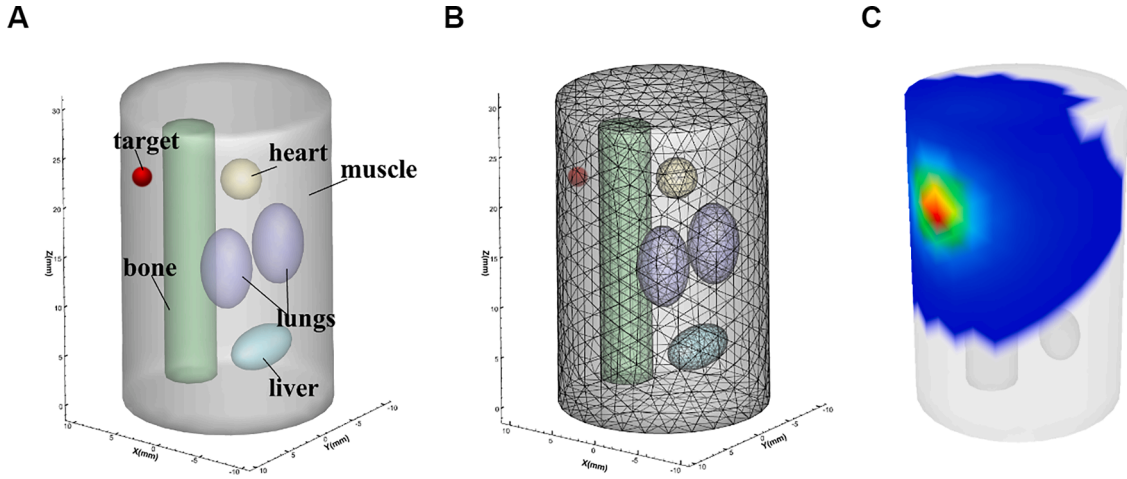
Fig. 1. A is a single-source phantom. B is tetrahedral mesh of physical model in BLT inverse problem. C is the surface bioluminescence distribution in the single light source simulation.

experiment settings and results.

3.1. Evaluation Metrics

To better evaluate the performance of the method in terms of reconstruction quality and accuracy, the Location error (LE) [50], Dice similarity coefficient (DICE) [51], Root Mean Square Error (RMSE) [52] and relative intensity error (RIE) [53] are adopted as quantitative evaluation metrics.

LE is the Euclidean distance between the reconstructed source center and the true source center. The definition is as follows:

$$LE = \| L_r - L_t \|_2 \tag{15}$$

where L_r and L_t represent the centers of the reconstructed target and the true target, respectively. The closer the LE is to 0, the higher the positioning accuracy.

The DICE coefficient is employed to evaluate the spatial structure similarity of the reconstructed source and the true source, which is defined as follows:

$$DICE = 2 \frac{|R_r \cap R_t|}{|R_r| + |R_t|} \tag{16}$$

where R_r and R_t represent the regions of the reconstructed target and the real target, respectively, DICE index ranges from 0 to 1. The closer the DICE is to 1, the higher the similarity between the reconstructed target and the real target.

The RMSE is defined as:

$$RMSE = \sqrt{\frac{\sum_N (X_r - X_t)}{N}} \tag{17}$$

where N is the number of nodes, X_r is the reconstructed bioluminescent source yield, and X_t is the ground truth. The RMSE is a measure of the difference between reconstructed and expected values. The smaller the RMSE, the better the reconstruction result.

RIE is used to evaluate the relative intensity error between the reconstructed bioluminescent source intensity and the actual source intensity:

$$RIE = \frac{|I_r - I_t|}{I_t} \tag{18}$$

where I_r and I_t represent the intensity of the reconstructed source and the true source. The closer the RIE is to 0, the better the intensity recovery of the reconstructed source.

Table 1

. Optical parameters of tissues and organs in a nonhomogeneous cylinder

| Tissue	$\mu_a(mm^{-1})$	$\mu_s(mm^{-1})$	g
Muscle	0.0052	10.80	0.90
Heart	0.0083	6.733	0.85
Lung	0.0133	19.70	0.90
Liver	0.0329	7.000	0.90
Bone	0.0060	60.09	0.90

3.2. Numerical simulation experiments

The non-uniform cylinder simulation object is shown in Fig. 1A. The cylinder has a radius of 10 mm and a height of 30 mm. The geometric model consists of five organs: heart, bone, liver, lung, and muscle, and the optical parameters of each organ are shown in Table 1. In the model, a small spherical radiation source with a diameter of 1mm is placed to represent the tumor. The photon wavelength is set to 650 nm to ensure proper penetration. In the reconstruction process, the anthropomorphic model is discretized into uniform tetrahedral meshes using the COMSOL multi-physical platform [54], which includes 4626 nodes and 25840 tetrahedral elements, as shown in Fig. 1B. To obtain forward simulation data, we use the Monte Carlo method to simulate the bioluminescence distribution of tissue surface using a molecular optical simulation environment (MOSE) [55]. The forward simulation results are shown in Fig. 1C.

Three groups of simulation experiments are carried out, and the forward simulation results are obtained by using MOSE software, and then the data near the light source are collected for reconstruction.

3.2.1. Single-source simulation result

In the single-source simulation, we placed a 1 mm radius sphere in the phantom to simulate the light source, with the center coordinates at (6, 5, 26) mm. Fig. 2A-D shows the reconstruction results of a single light source. The 3D reconstruction and the axial plane shape demonstrate the effectiveness of our proposed method. Table 2 presents the quantitative analysis results of the four methods. The experimental results show that compared with the FISTA, IVTCG, and L_1-TV methods, the PCG-logTV method has a smaller LE, which means that the reconstructed light source position is closer to the actual light source position. And there is a larger DICE, up to 0.883, which is 1.68times of FISTA, 1.46times of IVTCG and 1.57times of L_1-TV, which indicates that the reconstructed light source area overlaps the actual light source area better. In addition, this method also has smaller RMSE and RIE, indicating that the predicted value of the reconstructed light source has a smaller error in
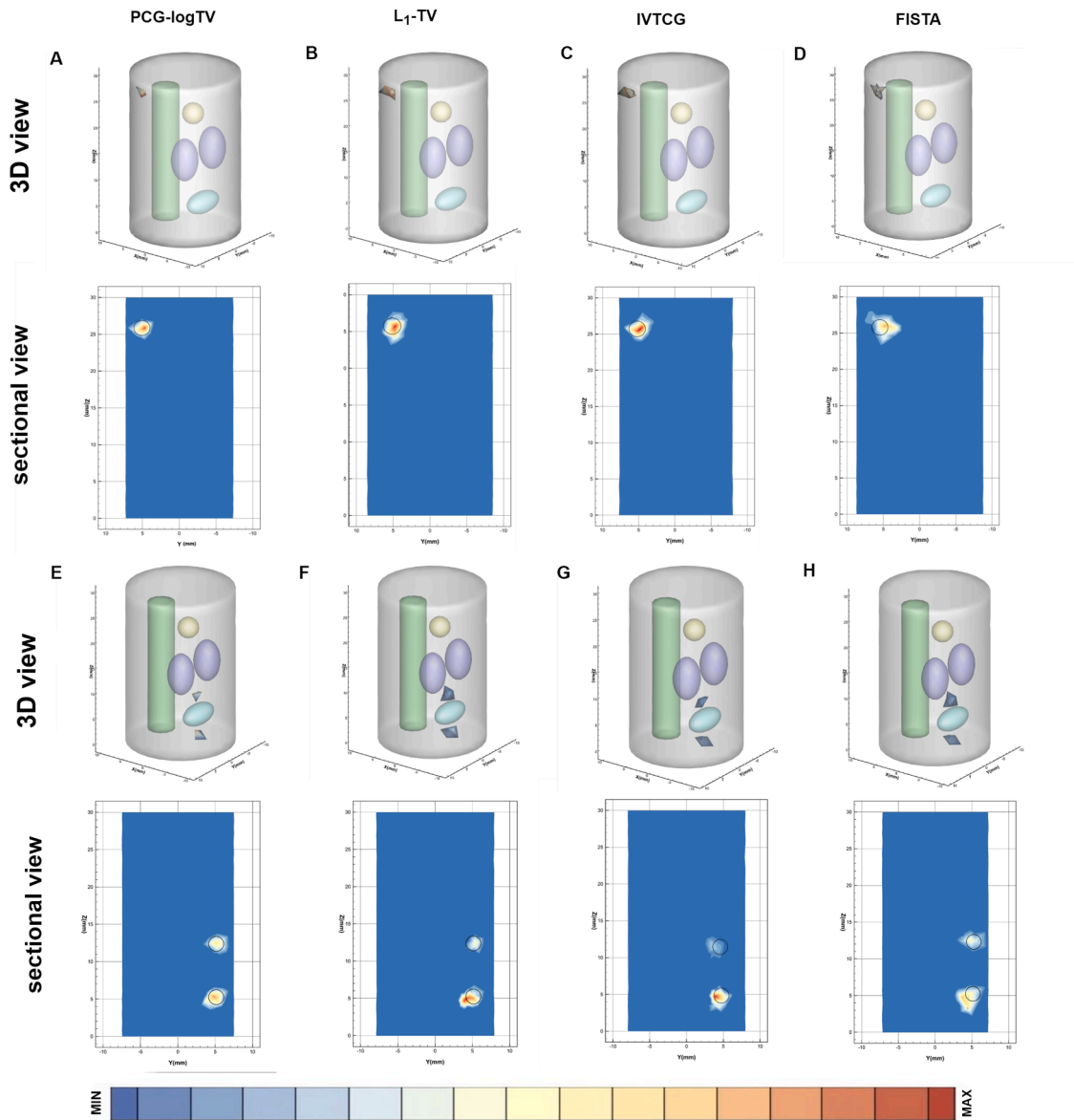
Fig. 2. comparison results of the light source simulation experiment (3D view and sectional view). A shows the reconstruction results of the PCG-logTV method for single source experiments. B-D are the results obtained by the L_1-TV method, IVTCG method and FISTA method for the single-source experiment. E-H presents the results reconstructed by PCG-logTV, L_1-TV, IVTCG and FISTA methods for the dual-source experiment. The red sphere in the cylindrical model represents the location of the true source, and the black circle on the axial view represents the true source under the axis view.

Table 2
Quantitative results in single-target simulation

Method	True (mm)	Results (mm)	LE (mm)	DICE	RMSE	RIE
FISTA	(6.0,5.0,26.0)	(6.742 5.591 25.847)	0.961	0.524	0.00419	0.980
IVTCG	(6.0,5.0,26.0)	(5.602 5.082 26.701)	0.810	0.605	0.00204	1.062
L_1-TV	(6.0,5.0,26.0)	(5.768,5.203,26.672)	0.739	0.571	0.00147	0.715
PCG-logTV	(6.0,5.0,26.0)	(5.830,4.926,25.813)	0.254	0.883	0.00072	0.194

intensity compared to the actual light source, and the intensity recovery of the reconstructed source is better. Therefore, the PCG-logTV method can reduce positional errors, improve average positioning accuracy, and largely reconstruct the spatial structure of the actual light source.

3.2.2. Dual-source simulation result

In the dual-source simulation, we placed two 1 mm radius spheres in the phantom, with the center coordinates at (-7, 5, 5) mm and (-7, 5, 12) mm, respectively. To assess the dual-source reconstruction ability of

PCG-logTV, we compared the reconstruction performance of PCG-logTV with other methods mentioned above. Fig. 2E-H illustrates the reconstruction results of dual light source simulation, and Table 3 reports the corresponding quantitative analysis results. According to the experimental results, the PCG-logTV method has smaller LE, RMSE, RIE, and larger DICE coefficients compared to other methods. This also indicates that the method has good light source localization and light source intensity reconstruction capabilities in the presence of different sources, and can accurately distinguish the positions of multiple light sources. At

Table 3
Quantitative results in dual-target simulation

Method	True (mm)	Results (mm)	LE (mm)	DICE	RMSE	RIE
FISTA	(-7.0,5.0,5.0)	(-6.794,4.482,4.503)	0.747	0.509	0.00507	0.730
	(-7.0,5.0,12.0)	(-7.529,5.607,11.540)	0.927	0.346	0.00362	1.017
IVTCG	(-7.0,5.0,5.0)	(-6.419,5.579,4.795)	0.846	0.472	0.00283	0.893
	(-7.0,5.0,12.0)	(-6.732,5.338,12.619)	0.745	0.583	0.00214	0.856
L_1-TV	(-7.0,5.0,5.0)	(-7.381,5.620,4.847)	0.744	0.481	0.00291	0.739
	(-7.0,5.0,12.0)	(-7.305,5.571,11.782)	0.612	0.519	0.00195	0.624
PCG-logTV	(-7.0,5.0,5.0)	(-6.820,4.860,4.765)	0.326	0.675	0.00208	0.176
	(-7.0,5.0,12.0)	(-6.90,4.539,12.015)	0.472	0.667	0.00185	0.151
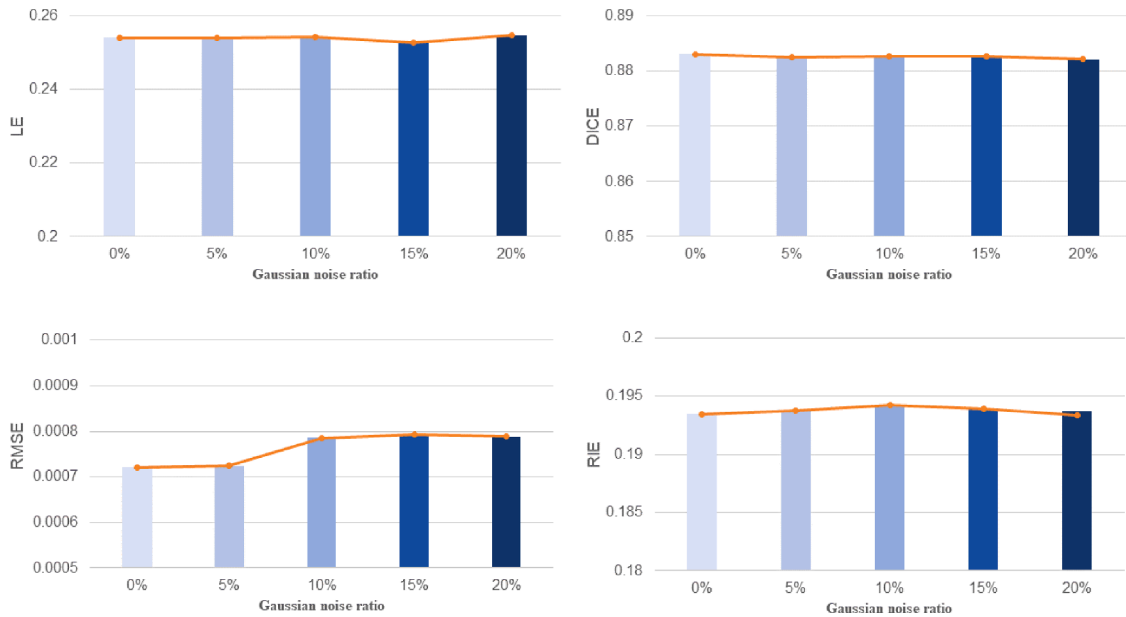
Fig. 3. Anti-noise experiment of BLT reconstruction.

the same time, the DICE coefficient results also indicate that the method has good spatial structure recovery ability.

3.2.3. Anti-noise experiment

To verify the stability of the PCG-logTV method, we conducted an anti-noise experiment. We used the single-source simulation as an example, with the light source coordinates at (6, 5, 26) mm, and added 5%, 10%, 15%, and 20% Gaussian noise to examine the impact on the PCG-logTV reconstruction results. Fig. 3 shows the changes in the four indicators under no noise and four Gaussian noise levels. According to the line chart corresponding to each indicator in Fig. 3, it can be seen that in the four sets of experiments, the relative changes of LE, DICE, RIE, and RMSE are relatively small, indicating that the method is robust to noise.

3.3. In vivo BLT reconstruction

To evaluate the practicability of our method *in vivo* imaging, we performed an in vivo xenograft mouse experiment. All experimental procedures were approved by the Animal Ethics Committee of Northwest University of China. We used an adult BALB/C mouse for the *in vivo* experiment. We anesthetized the mouse with 3% isoflurane-air mixture during animal surgery.

In this experiment, we imaged the adult nude mouse by a dual mode tomography system. To collect bioluminescence images, we used a 650 nm band-pass filter, operated the EMCCD player (IxonUltra888) at, set the exposure time to 1 second and no gain value. To obtain the anatomical structure, we used a miniature CT system (tube voltage
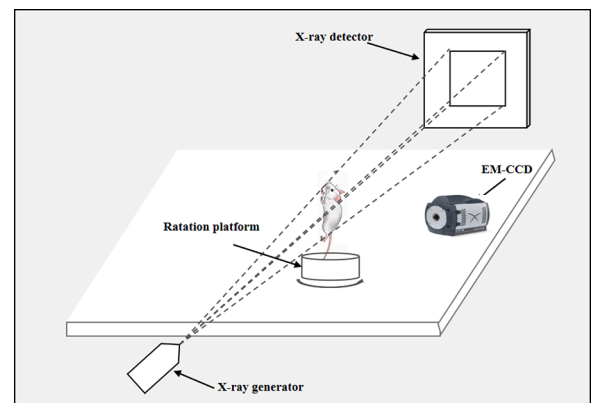
Fig. 4. The schematic diagram of a device structure of a dual-mode system.

Table 4
Optical parameters of tissues and organs *in vivo* mouse experiment.

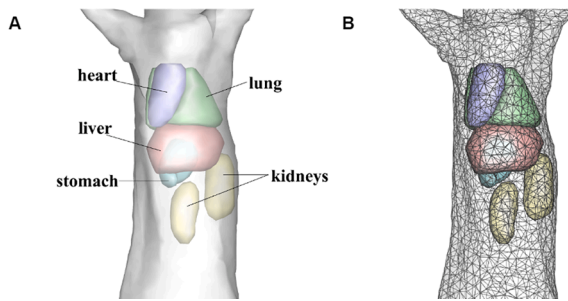| Tissue	$\mu_\alpha(mm^{-1})$	$\mu_s(mm^{-1})$	g
Muscle	0.016	5.10	0.9
Heart	0.011	10.53	0.86
Lung	0.002	15.25	0.90
Liver	0.065	7.23	0.90
Stomach	0.012	24.72	0.90
Kidney	0.036	22.46	0.90

Fig. 5. The *in vivo* mouse model is shown in Fig. 5A, and Fig. 5B shows the distribution of the light source at a certain location in the mouse body

Table 5
Quantitative analysis of *in vivo* reconstruction results

Method	True (mm)	LE (mm)	DICE	RMSE	RIE
FISTA	(14.5, 8.0, 22.6)	0.915	0.439	0.00794	0.852
IVTCG	(14.5, 8.0, 22.6)	0.823	0.476	0.00725	0.679
L_1-TV	(14.5, 8.0, 22.6)	0749	0.651	0.00908	0.571
PCG-logTV	(14.5, 8.0, 22.6)	0.330	0.928	0.00353	0.206

60kvp, X-ray power of 40W) for CT imaging. Fig. 4 shows the schematic diagram of the device structure of a BLT/micro-CT dual-mode system.

Next, we processed the collected data, and segmented the main organs, including muscle, lung, heart, stomach, liver, and kidney, according to the CT image, and integrated them into the mouse trunk model. Finally, we matched and registered the bioluminescence images to the surface of the mouse trunk model. Table 4 [56] shows the optical parameters of different organs used in the *in vivo* xenograft mouse experiment. We discretized the mouse model into 6869 nodes and 30659 tetrahedral elements for reconstruction, as Fig. 5 illustrates. The coordinate of the implanted real source was (14.5, 8.0, 22.6) mm. To assess the feasibility of this method *in vivo*, we also compared PCG-logTV with the other three algorithms mentioned above.

Table 5 presents the quantitative analysis of the reconstruction results of different methods, and Fig. 6 displays the three-dimensional and cross-sectional views. The quantitative analysis results indicate that compared with other methods, PCG-logTV outperforms all other

methods in terms of indicators. FISTA method has poor ability in light source localization and light source intensity reconstruction, IVTCG method lacks good spatial structure recovery ability, and L_1-TV method also performs poorly in light source intensity reconstruction. However, in the PCG-logTV method, the positional error between the reconstructed source and the actual source is relatively small, and a reasonable source shape is obtained, with a maximum overlap Dice of 0.928. The smaller RIE and RMSE indicate that PCG-logTV has a better reconstruction effect on light source intensity. The results demonstrate that the PCG-logTV method can effectively locate and recover light sources in space, and the reconstructed source has a clear shape. In addition, this method can effectively reduce the artifact area of reconstruction and has good reconstruction accuracy. This suggests that the PCG-logTV method has good practicability.

4. Discussion

BLT is a fast-growing endogenous three-dimensional imaging technology that can reconstruct the distribution of bioluminescent light sources by measuring surface luminous flux. However, due to the ill-posed nature of the reconstruction problem, the reconstruction quality is severely degraded. In this study, we propose a PCG-logTV method to overcome the ill-posedness of the BLT problem and achieve sparse reconstruction of BLT. This method combines TV regularization and logarithmic function. The TV regularization serves as a penalty function that effectively preserves edge information and discontinuity in BLT reconstruction. This ensures that the reconstructed images maintain sharpness and accuracy. Additionally, the logarithmic function is employed to avoid the trapezoidal artifacts commonly observed in total variation solutions. To reduce the condition number of the inverse problem and accelerate the convergence rate of the solution, we use the preconditioned conjugate gradient iterative method for the final objective function. This helps achieve faster and more stable reconstructions.

To assess the performance of the PCG-logTV method, we performed three sets of numerical simulations and an *in vivo* xenotransplantation experiment. quantitatively compared the results with other traditional reconstruction algorithms, namely FISTA, IVTCG, and L_1-TV methods. The simulation experiments involving single-source and double-source demonstrate that the PCG-logTV method can accurately recover the shape and spatial location of light sources. The noise-resilience
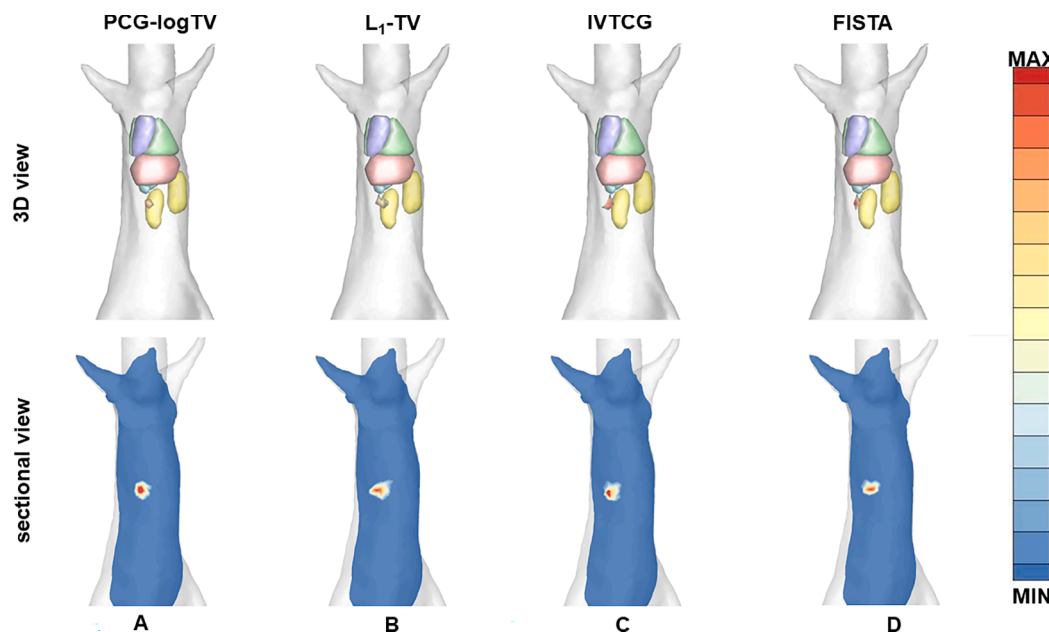

Fig. 6. Reconstruction results of different methods *in vivo* experiment. The black circles on the section diagram represent the actual source.

experimental results show that the PCG-logTV method is robust against noise. Furthermore, the in vivo experiment confirms the superior performance of the PCG-logTV method in all aspects, thus proving its feasibility for reconstructing light sources in living mouse.

However, despite the significant improvements achieved by the PCG-logTV method, it does have some limitations. Firstly, the linear search used in the PCG method increases the computation time of each iteration. Secondly, due to the addition of preprocessing conditions, the selection of the overrelaxation factor relies on experience, introducing subjectivity. Lastly, there may be some discrepancy between the shape of the reconstructed light source and the true light source. Therefore, further improvements to the algorithm's performance, a reduction in the number of iterations, and consideration of the actual light source's shape and overall structural information are needed.

5. Conclusion

In summary, we propose a PCG-logTV method that combines TV regularization and logarithm function for sparse reconstruction of BLT. The PCG-logTV method greatly reduces the ill-posedness of BLT reconstruction and avoids the staircase artifacts often seen in total variational solutions. We validate the algorithm through a series of numerical simulations and an in vivo xenograft mouse experiment, and compare it with other traditional reconstruction algorithms. The experimental results show that the PCG-logTV method exhibits excellent spatial positioning accuracy and shape recovery performance. This method effectively enhances the quality and accuracy of reconstruction results, achieving sparser and more stable reconstruction outcomes. We believe that this novel method will contribute to improving BLT reconstruction performance and facilitating various preclinical applications of BLT.

Disclosures

The authors declare no conflicts of interest.

Data availability

Data underlying the results presented in this paper are not publicly available at this time but may be obtained from the authors upon request.

Declaration of Competing Interest

The authors have declared no conflict of interest

Funding

References

[1] W. Yin, X. Li, Q. Cao, H. Wang, B. Zhang, Bioluminescence tomography reconstruction in conjunction with an organ probability map as an anatomical reference, Biomedical Optics Express 13 (3) (2022) 1275–1291.

[2] M.A. Naser, M.S. Patterson, Algorithms for bioluminescence tomography incorporating anatomical information and reconstruction of tissue optical properties, Biomedical optics express 1 (2) (2010) 512.

[3] J.K. Willmann, N. Van Bruggen, L.M. Dinkelborg, S.S. Gambhir, Molecular imaging in drug development, Nature reviews Drug discovery 7 (7) (2008) 591–607.

[4] C. Qin, J. Feng, S. Zhu, X. Ma, J. Zhong, P. Wu, Z. Jin, J. Tian, Recent advances in bioluminescence tomography: methodology and system as well as application, Laser & Photonics Reviews 8 (1) (2014) 94–114.

[5] H. Guo, J. Yu, Z. Hu, H. Yi, Y. Hou, X. He, A hybrid clustering algorithm for multiple-source resolving in bioluminescence tomography, Journal of biophotonics 11 (4) (2018), e201700056.

[6] V. Ntziachristos, J. Ripoll, L.V. Wang, R. Weissleder, Looking and listening to light: the evolution of whole-body photonic imaging, Nature biotechnology 23 (3) (2005) 313–320.

[7] Z. Hu, Y. Qu, K. Wang, X. Zhang, J. Zha, T. Song, C. Bao, H. Liu, Z. Wang, J. Wang, In vivo nanoparticle-mediated radiopharmaceutical-excited fluorescence molecular imaging, Nature communications 6 (1) (2015) 7560.

[8] Y. Gao, K. Wang, S. Jiang, Y. Liu, T. Ai, J. Tian, Bioluminescence tomography based on Gaussian weighted Laplace prior regularization for in vivo morphological imaging of glioma, IEEE transactions on medical imaging 36 (11) (2017) 2343–2354.

[9] H. Hu, J. Liu, L. Yao, J. Yin, N. Su, X. Liu, F. Cao, J. Liang, Y. Nie, K. Wu, Real-time bioluminescence and tomographic imaging of gastric cancer in a novel orthotopic mouse model, Oncology reports 27 (6) (2012) 1937–1943.

[10] S. Mollard, R. Fanciullino, S. Giacometti, C. Serdjebi, S. Benzekry, J. Ciccolini, In vivo bioluminescence tomography for monitoring breast tumor growth and metastatic spreading: comparative study and mathematical modeling, Scientific Reports 6 (1) (2016) 36173.

[11] J. Yu, B. Zhang, I.I. Iordachita, J. Reyes, Z. Lu, M.V. Brock, M.S. Patterson, J. W. Wong, K.K.H. Wang, Systematic study of target localization for bioluminescence tomography guided radiation therapy, Medical physics 43 (5) (2016) 2619–2629.

[12] J. Feng, K. Jia, Z. Li, B.W. Pogue, M. Yang, Y. Wang, Bayesian sparse-based reconstruction in bioluminescence tomography improves localization accuracy and reduces computational time, Journal of biophotonics 11 (4) (2018), e201700214.

[13] G. Wang, Y. Li, M. Jiang, Uniqueness theorems in bioluminescence tomography, Medical physics 31 (8) (2004) 2289–2299.

[14] Z. Hu, J. Liang, W. Yang, W. Fan, C. Li, X. Ma, X. Chen, X. Ma, X. Li, X. Qu, Experimental Cerenkov luminescence tomography of the mouse model with SPECT imaging validation, Optics express 18 (24) (2010) 24441–24450.

[15] A. Ale, V. Ermolayev, E. Herzog, C. Cohrs, M.H. De Angelis, V. Ntziachristos, FMT-XCT: in vivo animal studies with hybrid fluorescence molecular tomography–X-ray computed tomography, Nature methods 9 (6) (2012) 615–620.

[16] F. Stuker, C. Baltes, K. Dikaiou, D. Vats, L. Carrara, E. Charbon, J. Ripoll, M. Rudin, Hybrid small animal imaging system combining magnetic resonance imaging with fluorescence tomography using single photon avalanche diode detectors, IEEE transactions on medical imaging 30 (6) (2011) 1265–1273.

[17] D. Chen, S. Zhu, X. Chen, T. Chao, X. Cao, F. Zhao, L. Huang, J. Liang, Quantitative cone beam X-ray luminescence tomography/X-ray computed tomography imaging, Applied Physics Letters 105 (19) (2014), 191104.

[18] K. Liu, X. Yang, D. Liu, C. Qin, J. Liu, Z. Chang, M. Xu, J. Tian, Spectrally resolved three-dimensional bioluminescence tomography with a level-set strategy, JOSA A 27 (6) (2010) 1413–1423.

[19] Z. Hu, C. Fang, B. Li, Z. Zhang, C. Cao, M. Cai, S. Su, X. Sun, X. Shi, C. Li, First-in-human liver-tumour surgery guided by multispectral fluorescence imaging in the visible and near-infrared-I/II windows, Nature biomedical engineering 4 (3) (2020) 259–271.

[20] H. Zhang, L. Hai, J. Kou, Y. Hou, X. He, M. Zhou, G. Geng, OPK_SNCA: Optimized prior knowledge via sparse non-convex approach for cone-beam X-ray luminescence computed tomography imaging, Computer Methods and Programs in Biomedicine 215 (2022), 106645.

[21] C. Li, G.S. Mitchell, S.R. Cherry, Cerenkov luminescence tomography for small-animal imaging, Optics letters 35 (7) (2010) 1109–1111.

[22] M. Cai, Z. Zhang, X. Shi, J. Yang, Z. Hu, J. Tian, Non-negative iterative convex refinement approach for accurate and robust reconstruction in Cerenkov luminescence tomography, IEEE transactions on medical imaging 39 (10) (2020) 3207–3217.

[23] Q. Zhang, H. Zhao, D. Chen, X. Qu, X. Chen, X. He, W. Li, Z. Hu, J. Liu, J. Liang, Source sparsity based primal-dual interior-point method for three-dimensional bioluminescence tomography, Optics Communications 284 (24) (2011) 5871–5876.

[24] H. Guo, Z. Hu, X. He, X. Zhang, M. Liu, Z. Zhang, X. Shi, S. Zheng, J. Tian, Non-convex sparse regularization approach framework for high multiple-source resolution in cerenkov luminescence tomography, Optics Express 25 (23) (2017) 28068–28085.

[25] N. Cao, A. Nehorai, M. Jacobs, Image reconstruction for diffuse optical tomography using sparsity regularization and expectation-maximization algorithm, Opt. express 15 (21) (2007) 13695–13708.

[26] C. Chen, F. Tian, H. Liu, J. Huang, Diffuse optical tomography enhanced by clustered sparsity for functional brain imaging, IEEE transactions on medical imaging 33 (12) (2014) 2323–2331.

[27] O. Scherzer, Handbook of mathematical methods in imaging, Springer Science & Business Media, 2010.

[28] A. Chambolle, An algorithm for total variation minimization and applications, Journal of Mathematical imaging and vision 20 (2004) 89–97.

[29] R. Chartrand, V. Staneva, Total variation regularisation of images corrupted by non-Gaussian noise using a quasi-Newton method, IET Image Processing 2 (6) (2008) 295–303.

[30] T.F. Chan, S. Osher, J. Shen, The digital TV filter and nonlinear denoising, IEEE Transactions on Image processing 10 (2) (2001) 231–241.

[31] D. Bertsekas, Nonlinear Programming, 2nd edn, Athena Scientific, Belmont, MA, 1999.

[32] J. Bect, L. Blanc-Féraud, G. Aubert, and A. Chambolle, "A l 1-unified variational framework for image restoration." pp. 1-13.

[33] J.P. Oliveira, J.M. Bioucas-Dias, M.A. Figueiredo, Adaptive total variation image deblurring: a majorization–minimization approach, Signal processing 89 (9) (2009) 1683–1693.

[34] Y. Wang, J. Yang, W. Yin, Y. Zhang, A new alternating minimization algorithm for total variation image reconstruction, SIAM Journal on Imaging Sciences 1 (3) (2008) 248–272.

[35] S. Osher, L. Vese, Image denoising and decomposition with total variation minimization and oscillatory functions. Special issue on mathematics and image analysis, J. Math. Imaging Vision 20 (1-2) (2004) 7–18.

[36] M. Zibulevsky, M. Elad, L1-L2 optimization in signal and image processing, IEEE Signal Processing Magazine 27 (3) (2010) 76–88.

[37] M. Hintermüller, M. Holler, K. Papafitsoros, A function space framework for structural total variation regularization with applications in inverse problems, Inverse Problems 34 (6) (2018), 064002.

[38] H. Guo, J. Yu, X. He, H. Yi, Y. Hou, Total Variation Constrained Graph Manifold Learning Strategy for Cerenkov Luminescence Tomography, Optics Express 30 (2) (2022) 1422–1441.

[39] R. Campagna, S. Crisci, S. Cuomo, L. Marcellino, G. Toraldo, Modification of TV-ROF denoising model based on Split Bregman iterations, Applied Mathematics and Computation 315 (2017) 453–467.

[40] I. W. Selesnick, and P.-Y. Chen, "Total variation denoising with overlapping group sparsity." pp. 5696-5700.

[41] A. Sant, M. Leinonen, B.D. Rao, Block-Sparse Signal Recovery via General Total Variation Regularized Sparse Bayesian Learning, IEEE Transactions on Signal Processing 70 (2022) 1056–1071.

[42] J.A. Fessler, S.D. Booth, Conjugate-gradient preconditioning methods for shift-variant PET image reconstruction, IEEE transactions on image processing 8 (5) (1999) 688–699.

[43] A. Beck, M. Teboulle, A fast iterative shrinkage-thresholding algorithm for linear inverse problems, SIAM journal on imaging sciences 2 (1) (2009) 183–202.

[44] X. He, J. Liang, X. Wang, J. Yu, X. Qu, X. Wang, Y. Hou, D. Chen, F. Liu, J. Tian, Sparse reconstruction for quantitative bioluminescence tomography based on the incomplete variables truncated conjugate gradient method, Optics Express 18 (24) (2010) 24825–24841.

[45] T. Liu, J. Rong, P. Gao, H. Pu, W. Zhang, X. Zhang, Z. Liang, H. Lu, Regularized reconstruction based on joint L 1 and total variation for sparse-view cone-beam x-ray luminescence computed tomography, Biomedical optics express 10 (1) (2019) 1–17.

[46] A.X. Cong, G. Wang, A finite-element-based reconstruction method for 3D fluorescence tomography, Optics Express 13 (24) (2005) 9847–9857.

[47] P. Wu, K. Liu, Q. Zhang, Z. Xue, Y. Li, N. Ning, X. Yang, X. Li, J. Tian, Detection of mouse liver cancer via a parallel iterative shrinkage method in hybrid optical/microcomputed tomography imaging, Journal of biomedical optics 17 (12) (2012), 126012-126012.

[48] J. Dutta, S. Ahn, C. Li, S.R. Cherry, R.M. Leahy, Joint L1 and total variation regularization for fluorescence molecular tomography, Physics in Medicine & Biology 57 (6) (2012) 1459.

[49] Z. Meng, F. Li, X. Xu, D. Huang, D. Zhang, Fast inversion of gravity data using the symmetric successive over-relaxation (SSOR) preconditioned conjugate gradient algorithm, Exploration Geophysics 48 (3) (2017) 294–304.

[50] H. Guo, L. Gao, J. Yu, X. He, H. Wang, J. Zheng, X. Yang, Sparse-graph manifold learning method for bioluminescence tomography, Journal of biophotonics 13 (4) (2020), e201960218.

[51] L. Yin, K. Wang, T. Tong, Q. Wang, Y. An, X. Yang, J. Tian, Adaptive grouping block sparse Bayesian learning method for accurate and robust reconstruction in bioluminescence tomography, IEEE Transactions on Biomedical Engineering 68 (11) (2021) 3388–3398.

[52] S. Li, X. He, H. Zhang, H. Guo, and X. He, "End-to-end bioluminescence tomography reconstruction based on convolution neural network scheme." pp. 3634-3639.

[53] Y. Chen, M. Du, W. Li, L. Su, H. Yi, F. Zhao, K. Li, L. Wang, X. Cao, ABPO-TVSCAD: alternating Bregman proximity operators approach based on TVSCAD regularization for bioluminescence tomography, Physics in Medicine & Biology 67 (21) (2022), 215013.

[54] B. Parvitte, C. Risser, R. Vallon, V. Zéninari, Quantitative simulation of photoacoustic signals using finite element modelling software, Applied Physics B 111 (2013) 383–389.

[55] N. Ren, J. Liang, X. Qu, J. Li, B. Lu, J. Tian, GPU-based Monte Carlo simulation for light propagation in complex heterogeneous tissues, Optics express 18 (7) (2010) 6811–6823.

[56] G. Alexandrakis, F.R. Rannou, A.F. Chatziioannou, Tomographic bioluminescence imaging by use of a combined optical-PET (OPET) system: a computer simulation feasibility study, Physics in Medicine & Biology 50 (17) (2005) 4225.